(Received 28 February 2024, Accepted 19 May 2024, Scheduled 9 July 2024)

Improved Orthogonal Flux Corrector-Based Rotor Flux Estimation in PMSM Sensorless Control

Siyuan Cheng[1, 2], Haoze Wang[3], and Yajie Jiang[4, *]

[1] *Department of Electrical, Computer and Software Engineering, The University of Auckland, Auckland, New Zealand*
[2] *State Grid Henan Electric Power Research Institute, Zhengzhou 450002, China*
[3] *POWERCHINA Central China Electric Power Engineering Co., Ltd., Zhengzhou 450000, China*
[4] *School of Electrical and Electronic Engineering, Nanyang Technological University, Singapore*

ABSTRACT: In a permanent magnet synchronous machine (PMSM) system, the voltage mode-based rotor flux observer suffers from DC drift, primarily due to measurement errors, parameter variations, and non-zero initial states. To address this issue, the second-order flux observer (SOFO) is utilized, equipped with filtering capability aimed at reducing harmonic components. However, the DC offset induced by external disturbances cannot be completely eliminated by the second-order transfer function alone. Traditional magnetic flux correctors typically update correction values only at zero-crossing points of the magnetic flux. In this study, we propose an improved orthogonal flux corrector (IOFC) that combines a generalized integrator to effectively filter out the DC offset. In comparison with traditional OFC methods, our approach involves reconstructing two magnetic linkage functions, thereby doubling the correction frequency within a single cycle. Consequently, the frequency of correction term updates is threefold compared to conventional OFC methods. Finally, IOFC is implemented and tested on a PMSM platform for experimental verification.

1. INTRODUCTION

With the merit of low-cost, the sensorless drive strategies in permanent magnet synchronous machine (PMSM) systems are widely studied [1–4]. Among common strategies, signal injection method suffers from the additional noises [5]. Moreover, signal injection and back electromotive force (EMF)-observation methods have limited applicable speed ranges [6]. The rotor position is consistent with the direction of the permanent magnet flux, yielding another rotor position extraction method. In view of rotor flux amplitude depends on the permanent magnet flux, and its amplitude remains unchanged under different speeds and loads. After comparisons, it is found that the rotor flux observation strategy exhibits remarkable advantages, such as wide speed range and strong parameter robustness [7].

The PMSM model can be constructed using stator voltages and fluxes, based on either voltage or current. In stationary coordinates, the rotor flux can be derived from both voltage-based and current-based models. However, the current-based model necessitates knowledge of the rotor position to estimate the flux, rendering it unsuitable for sensorless drive [8]. Additionally, time delays in the feedback loop may lead to system instability and observation failures. For voltage-based estimation, a straightforward approach involves acquiring the rotor flux through integration stages [9]. The simplest integrator is a first-order integrator, though it may lead to saturation phenomena. In the case of a low-pass filter (LPF), if the motor's actual operating frequency approaches or exceeds the filter cut-off frequency, the phase information of the estimated rotor flux may vary, and its amplitude may decrease. Furthermore, the presence of non-ideal interference variables such as DC bias within the system can diminish the accuracy of position sensorless control algorithms.

In efforts to eliminate harmonics and DC offsets, several studies have sought to mathematically model and compensate for non-ideal flux components. Some researchers have proposed enhanced flux observers, such as the disturbance observer (DOB) [10] and the second-order generalized integrator (SOGI) [11], to mitigate DC offsets. However, the second-order flux observer (SOFO) struggles to effectively suppress the influence of DC disturbances originating from the initial integration value [12]. Recently, a limit cycle oscillator is employed to confine the acquired flux cycle. However, the intricate structures of both the SOFO and oscillator limit their practical application [13]. Alternatively, orthogonal flux corrector (OFC) is proposed in [14] based on zero-crossing correction. By employing a properly designed closed-loop system, an offset signal can be extracted for compensation. However, the correction term for each rotor flux (either α-axis or β-axis) can be only updated twice within a cycle. This low-frequency update strategy complicates the design of parameters for closed-loops, as it fails to strike a balance between dynamic response and steady-state offset tracking.

This paper demonstrates that SOFO is sensitive to DC disturbances. To address this issue and eliminate DC offsets, we propose an improved orthogonal flux corrector (IOFC). Specifically, the phase and amplitude between two orthogonal magnetic flux chains, which maintain constant amplitudes, are uti-

* Corresponding author: Yajie Jiang (u3005844@connect.hku.hk).

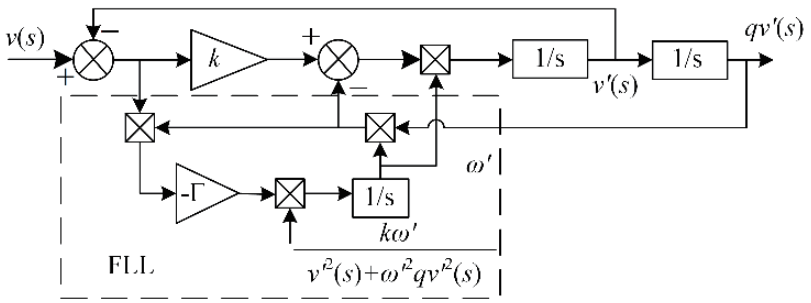

FIGURE 1. Block diagram of SOFO-FLL.

lized for correction. Additionally, two additional orthogonal flux signals are established to provide additional correction updates. Through the proportional-integral (PI) controllers, the DC bias is extracted and utilized for signal correction. Compared to conventional orthogonal flux correctors (OFC), the designed IOFC offers both rapid dynamic response and precise steady-state tracking simultaneously. Finally, we validate the effectiveness of the IOFC through experimental implementation on a PMSM drive platform.

2. ROTOR FLUX OBSERVATION

The PMSM model can be given as follows [8]

$$\mathbf{u}_s = R_s \cdot \mathbf{i}_s + e_s = R_s \cdot \mathbf{i}_s + pL_s \cdot \mathbf{i}_s + p\psi_f \quad (1)$$

$$\psi_{r\alpha} = \psi_f \cos(\theta_e), \quad \psi_{r\beta} = \psi_f \sin(\theta_e) \quad (2)$$

where $\boldsymbol{u}_s = [u_\alpha \quad u_\beta]^{\mathrm{T}}$ are stator voltages; $\boldsymbol{i}_s = [i_\alpha \quad i_\beta]^{\mathrm{T}}$ are stator currents; $\psi_r = [\psi_{r\alpha} \quad \psi_{r\beta}]^{\mathrm{T}}$ are rotor fluxes; $\boldsymbol{e}_s = [e_\alpha \quad e_\beta]^{\mathrm{T}}$ are EMFs; L_s is the inductance; R_s is the stator resistance; θ_e is the rotor electrical position; p is the differential operator; ψ_f is the rotor flux linkage; ω_e is the rotor electrical angular velocity. Based on (1), the flux observer and position can be given as

$$p\hat{\psi}_r = \mathbf{u}_s - R_s\mathbf{i}_s - L \cdot p\mathbf{i}_s \quad (3)$$

$$\hat{\theta}_e = \tan^{-1}(\hat{\psi}_{r\beta}/\hat{\psi}_{r\alpha}), \quad \hat{\omega}_e = p\hat{\theta}_e \quad (4)$$

where $\hat{\psi}_r = [\ \hat{\psi}_{r\alpha} \quad \hat{\psi}_{r\beta}\ ]^T$ are estimated rotor flux, and $\hat{\omega}_e$ and $\hat{\theta}_e$ are estimated velocity and position, respectively.

Intuitively, the rotor flux (which contains rotor position information) can be obtained by integrating the voltages. However, in practice, the first-order integrator tends to generate DC offset and harmonics. Taking into account these non-ideal components, the EMFs are then given as

$$\mathbf{e}_r(t) = \mathbf{A}_0 + \mathbf{A}_1 \sin(\omega_1 t + \varphi_1) + \sum \mathbf{A}_h \sin(\omega_h t + \varphi_h) \quad (5)$$

where $\boldsymbol{A}_0 = [A_{0\alpha} \ A_{0\beta}]^{\mathrm{T}}$, $\boldsymbol{A}_1 = [A_{1\alpha} \ A_{1\beta}]^{\mathrm{T}}$, and $\boldsymbol{A}_h = [A_{h\alpha} \quad A_{h\beta}]^{\mathrm{T}}$ are the amplitudes of DC component, fundamental component, and harmonics; φ_1 is the initial angel of fundamental waveform; φ_h is the initial angel of h-order harmonics; ω_1 is the angular of fundamental component; ω_h is the angular frequency of h-order harmonics; h is the harmonic orders. By adopting the Laplace transform, it yields

$$\mathbf{E}_r(s) = \frac{\mathbf{A}_0}{s} + \mathbf{A}_1 \frac{s\sin(\varphi_1) + \omega_1 cos(\varphi_1)}{s^2 + \omega_1^2} + \sum \mathbf{A}_h \frac{s\sin(\varphi_h) + \omega_h cos(\varphi_h)}{s^2 + \omega_h^2} \quad (6)$$

where s is the Laplace operator, and $\boldsymbol{E}_r(s)$ is the complex frequency domain form of $\boldsymbol{e}_r$.

The SOFO combined with frequency locked loop (FLL) is proposed in [2], as plotted in Figure 1.

By using the final-value theorem, $Q(s)$ can be rewritten by applying $s{=}j\omega'$:

$$Q(s) = \frac{qv'(s)}{v(s)} = \frac{k\omega'^2}{s^2 + k\omega' s + \omega'^2} = \frac{k\omega'^2}{-\omega'^2 + k\omega' s + \omega'^2} = \frac{\omega'}{s} \quad (7)$$

By combining the transfer function with (7), the estimated rotor flux in frequency domain is given as

$$\psi_{r\_SOFO}(s) = \frac{\mathbf{A}_0 k}{\omega_1} + \frac{\mathbf{A}_1}{\omega_1}\sin(\omega_1 t + \varphi_1 - 0.5\pi) + \sum \frac{\mathbf{A}_h}{\omega_h} \frac{\sin(\omega_h t + \varphi_h - 0.5\pi + \gamma_{h1})}{\sqrt{\frac{(1-h^2)^2}{k^2h^2} + 1}} \quad (8)$$

where $\psi_{r\_SOFO} = [\psi_{r\alpha\_SOFO}(s) \quad \psi_{r\beta\_SOFO}(s)]^{\mathrm{T}}$, $\omega_1 = \omega'$ the center frequency of SOFO, $h = \omega_h/\omega'$, and $\gamma_{h1} = \arctan[(\omega'^2 - \omega_h^2)/k\omega'\omega_h]$. In (8), the DC component is limited within $\mathbf{A}_0 k/\omega_1$, and k is a coefficient. However, when external DC disturbances are injected, the conducted DC drift cannot be eliminated by SOFO.

3. ORTHOGONAL FLUX CORRECTOR

3.1. Conventional OFC

Ideally, the rotor flux of a PMSM in $\alpha\beta$-axis can be given by two orthogonal sinusoidal signals in (2). In practice, the estimated flux always drifts due to reasons such as the imperfection of the driving current and the bias of sensors.

Thereby, the orthogonal signals are given as

$$\psi_{ra1} = \psi_{ra} + d_\alpha \quad \psi_{r\beta 1} = \psi_{r\beta} + d_\beta \tag{9}$$

where d_α and d_β denote the drifts, which are basically signals proportional to external disturbance.

To address the issue of drifts, the OFC is proposed. The detailed principle can be summarized as follows: under specific phase angles, the values of two orthogonal signals should match predetermined values. The correction terms, denoted as μ_α and μ_β, are defined for the fluxes $\psi_{r\alpha}$ and $\psi_{r\beta}$, respectively. The detailed generation processes for various conditions are provided below.

① When $\psi_{r\alpha}$ changes from positive to negative, $\psi_{r\beta}$ should be the maximum (positive) value: $\psi_{r\beta} = \psi_f$, which yields

$$\mu_\beta = \psi_{r\beta 1} - \sqrt{\left|\psi_f^2 - \psi_{r\alpha 1}^2\right|} \tag{10a}$$

② When $\psi_{r\beta}$ changes from positive to negative, $\psi_{r\alpha}$ should be the minimum (negative) value: $\psi_{r\alpha} = -\psi_f$, which yields

$$\mu_\alpha = \psi_{r\alpha 1} + \sqrt{\left|\psi_f^2 - \psi_{r\beta 1}^2\right|} \tag{10b}$$

③ When $\psi_{r\alpha}$ changes from negative to positive, $\psi_{r\beta}$ should be the minimum (negative) value: $\psi_{r\beta} = -\psi_f$, which yields

$$\mu_\beta = \psi_{r\beta 1} + \sqrt{\left|\psi_f^2 - \psi_{r\alpha 1}^2\right|} \tag{10c}$$

④ When $\psi_{r\beta}$ changes from negative to positive, $\psi_{r\alpha}$ should be the maximum (positive) value: $\psi_{r\alpha} = \psi_f$, which yields

$$\mu_\alpha = \psi_{r\alpha 1} - \sqrt{\left|\psi_f^2 - \psi_{r\beta 1}^2\right|} \tag{10d}$$

In (10), the correction points of each flux can only be updated twice within one cycle. The correction points of traditional OFC are plotted in Figure 2.

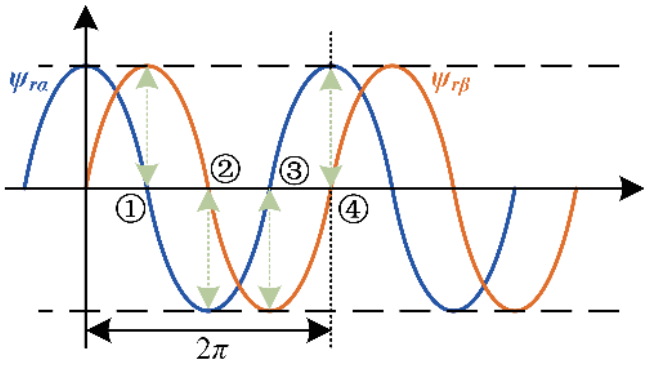

FIGURE 2. Correction points of conventional OFC within one cycle.

3.2. Proposed IOFC

Here, based on the original rotor flux, two new frequency-doubling orthogonal signals are established to increase the correction-updating frequency. With the help of addition angle formulas, it obtains

$$\begin{aligned} f_\alpha &= \hat{\psi}_{r\alpha} + \hat{\psi}_{r\beta} = \psi_f \cos(\theta_e) + \psi_f \sin(\theta_e) \\ &= \sqrt{2}\psi_f \sin(\theta_e + \pi/4) \end{aligned} \tag{11a}$$

$$\begin{aligned} f_\beta &= -\hat{\psi}_{r\alpha} + \hat{\psi}_{r\beta} = \psi_f \sin(\theta_e) - \psi_f \cos(\theta_e) \\ &= \sqrt{2}\psi_f \sin(\theta_e - \pi/4) = \sqrt{2}\psi_f \cos(\theta_e + \pi/4) \end{aligned} \tag{11b}$$

According to (11), the increased updating conditions are given as follows.

⑤ When f_β changes from negative to positive, f_α should be the maximum (positive) value: $f_\alpha = \sqrt{2}\psi_f$, which yields

$$\mu_\alpha^{'} = f_\alpha - \sqrt{\left|2\psi_f^2 - f_\beta^2\right|} \tag{12a}$$

Meanwhile, the actual two fluxes should be positive and equal to each other: $\psi_{r\alpha} = \psi_{r\beta} = \psi_f/\sqrt{2}$, which yields

$$\mu_\alpha = \psi_{r\alpha 1} - \psi_f/\sqrt{2}; \quad \mu_\beta = \psi_{r\beta 1} - \psi_f/\sqrt{2} \tag{12b}$$

⑥ When f_α changes from positive to negative, f_β should be the maximum (positive) value: $f_\beta = \sqrt{2}\psi_f$, which yields

$$\mu_\beta^{'} = f_\beta - \sqrt{\left|\psi_f^2 - f_\alpha^2\right|} \tag{12c}$$

while the actual two axis magnetic fluxes should be opposite to each other: $\psi_{r\alpha} = -\psi_f/\sqrt{2}$ and $\psi_{r\beta} = \psi_f/\sqrt{2}$, which yields

$$\mu_\alpha = \psi_{r\alpha 1} + \psi_f/\sqrt{2}; \quad \mu_\beta = \psi_{r\beta 1} - \psi_f/\sqrt{2} \tag{12d}$$

⑦ When f_β changes from positive to negative, f_α should be the minimum (negative) value: $f_\alpha = -\sqrt{2}\psi_f$, which yields

$$\mu_\alpha^{'} = f_\alpha + \sqrt{\left|2\psi_f^2 - f_\beta^2\right|} \tag{12e}$$

Meanwhile, the actual two fluxes should be negative and equal to each other: $\psi_{r\alpha} = \psi_{r\beta} = -\psi_f/\sqrt{2}$, which yields

$$\mu_\alpha = \psi_{r\alpha 1} + \psi_f/\sqrt{2}; \mu_\beta = \psi_{r\beta 1} + \psi_f/\sqrt{2} \tag{12f}$$

⑧ When f_α changes from negative to positive, f_β should be the minimum (negative) value: $f_\beta = -\sqrt{2}\psi_f$, which yields

$$\mu'_\beta = f_\beta + \sqrt{\left|\psi_f^2 - f_\alpha^2\right|} \tag{12g}$$

while the actual two axis magnetic fluxes should be opposite to each other: $\psi_{r\alpha} = \psi_f/\sqrt{2}$, and $\psi_{r\beta} = -\psi_f/\sqrt{2}$, which yields

$$\mu_\alpha = \psi_{r\alpha 1} - \psi_f/\sqrt{2}; \mu_\beta = \psi_{r\beta 1} + \psi_f/\sqrt{2} \tag{12h}$$

Herein, all correction actions numbered ①–⑧ are included in the proposed IFOC. In (12) and Figure 3, the correction points of each flux will be updated by six times within one cycle. In other words, the correction frequency of proposed IOFC is three times that of the original OFC.

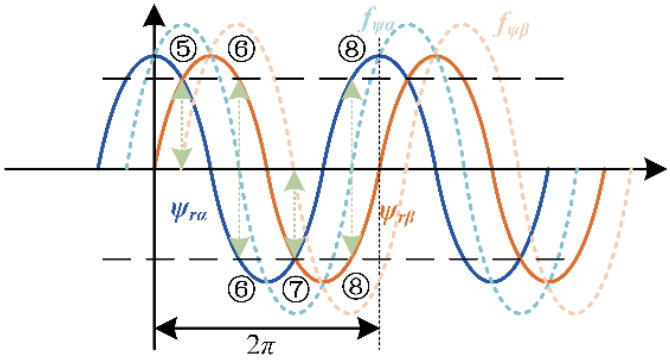

FIGURE 3. Increased correction points of proposed IOFC within one cycle.

The diagram of proposed IOFC is plotted in Figure 4. Once an updating condition is detected, the generated correction values are input into the integrator and PI regulator. Consequently, the DC component can be acquired and utilized for further compensation. The resulting rotor fluxes $\psi_{r\alpha1}$ and $\psi_{r\beta1}$ are then employed for sensorless drives. With IOFC, the flux observer can effectively operate across a wide range of PI regulator parameters, enabling both fast dynamic response and precise steady-state tracking simultaneously.

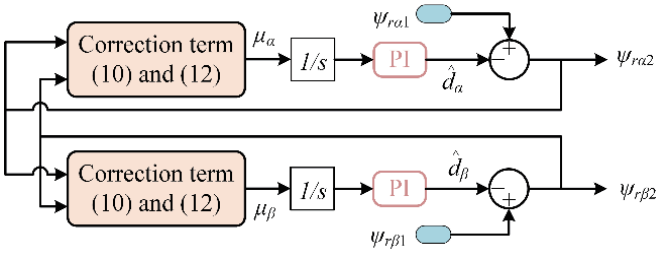

FIGURE 4. Diagram of proposed IOFC.

3.3. Analysis and Parameter Design

In the convergence analysis, the estimated offsets in $\alpha\beta$-axis are given as $\hat{d}_\alpha$ and $\hat{d}_\beta$, respectively. The drift estimation errors are defined as

$$d_{e\alpha} = d_\alpha - \hat{d}_\alpha, \quad d_{e\beta} = d_\beta - \hat{d}_\beta \tag{13}$$

Taking the estimation error in β-axis as an example, its derivative is given as

$$\dot{d}_{e\beta} = \dot{d}_\beta - \dot{\hat{d}}_\alpha = \dot{d}_\beta - \frac{k_p s + k_i}{s}\mu_\beta \tag{14}$$

where $\mu_\beta = \psi_{r\beta} + d_\beta \pm \sqrt{\left|\psi_f^2 - (\psi_{r\alpha} + d_\alpha)^2\right|}$.

Because the offset is DC component, $\dot{d}_\beta = 0$. It can be assumed that the estimation error in α-axis is zero, and it obtains $\mu_\beta \approx d_\beta$. Combining above equations obtains

$$\ddot{d}_{e\beta} = -k_p \dot{d}_\beta - k_i d_\beta \tag{15}$$

With the integrator and PI regulator, (15) is a classic second-order dynamic equation, which yields observation error that converges to 0 exponentially. Similarly, it can be derived that observation error in α-axis will also converge to 0, under the assumption of $d_\beta \approx 0$. Additionally, the amplitude of DC bias (d_α and d_β) should be limited to prevent correction failure. The IOFC-based sensorless drive strategy is implemented, as shown in Figure 5.

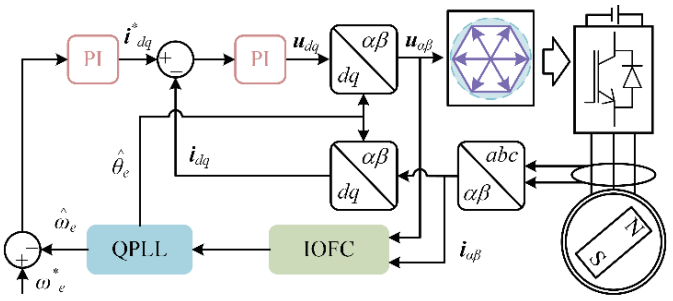

FIGURE 5. Diagram of the proposed sensorless control strategy.

4. CASE STUDIES

For experimental validation, the proposed IOFC strategy undergoes testing on a machine drive platform, as shown in Figure 6. The key parameters of the adopted PMSM are detailed in Table 1. This platform incorporates an induction motor (referred to as the load motor) and a PMSM, which is connected through a torque sensor. One uncontrolled rectifier serves as the DC power supply. Utilizing the STM32H750IBT6 microprocessor, both motors are controlled by a four-quadrant converter. Operating at the switching frequency of 10 kHz, the state variables of the motors are sampled and collected in real-time. Subsequently, the data is transmitted to an upper computer via the Controller Area Network (CAN) protocol. Following the collection of state variables, the data is displayed using an oscilloscope.

TABLE 1. Main parameters of PMSM.

Symbol	Quantity	Value and Unit
Ψ_f	Flux linkage of permanent magnet	0.22 Wb
n_p	Pole pairs	4
R_s	Stator resistance	0.493 Ω
P_N	Rated power	2.3 kW
n_N	Rated speed	1500 rpm
L_s	Stator inductances	2 mH
V_N	Rated voltage	380 V
I_N	Rated current	9.7 A

4.1. Performance under DC Disturbance

Under the external DC disturbance of $\Delta u_\beta = +30$ V, the experimental waveforms of SOFO, OFC, and proposed IOFC are

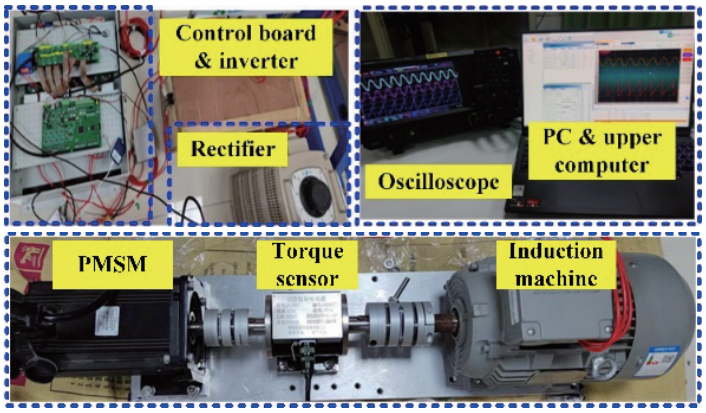

FIGURE 6. PMSM experimental setup.

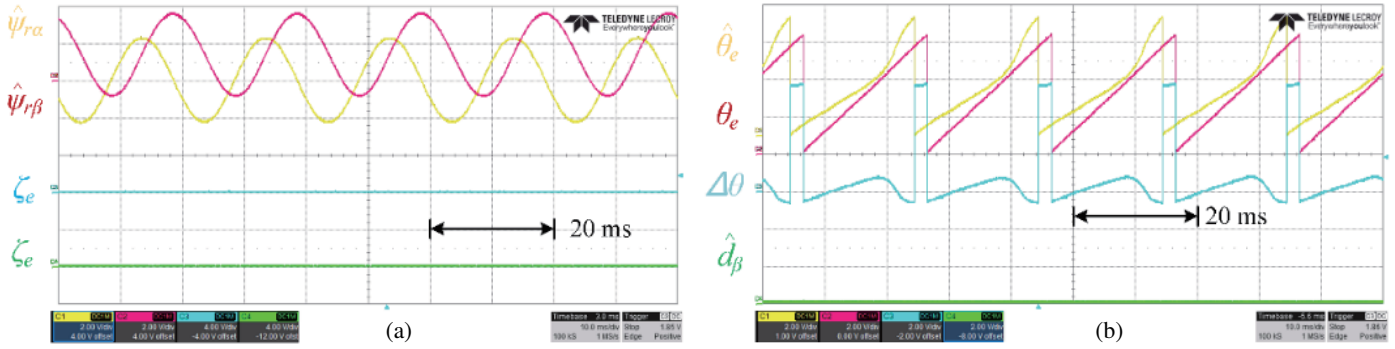

FIGURE 7. Waveforms by SOFO: (a) observed rotor flux and correction points, (b) rotor position and estimated DC component.

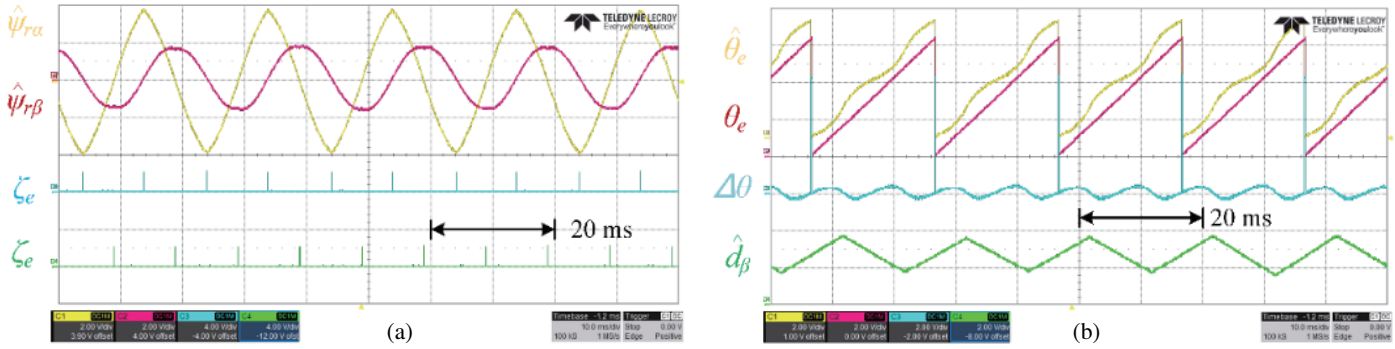

FIGURE 8. Waveforms by OFC: (a) observed rotor flux and correction points, (b) rotor position and estimated DC component.

shown in Figures 7, 8, and 9, respectively. Furthermore, the flux correction-triggered times for $\psi_{r\alpha}$ and $\psi_{r\beta}$ are defined as ζ_α and ζ_β, respectively. For clear comparison, ζ_α and ζ_β by conventional OFC and IOFC are also presented in Figures 7, 8, and 9. In Figure 7, by using conventional SOFO, no correction point can be observed, while the correction term is zero. As a result, the DC offset (0.13 Wb) can be observed from the estimated $\hat{\psi}_{r\beta}$. Meanwhile, the estimated rotor position cannot be used for PMSM drives. In Figure 8, by using conventional OFC, large fluctuation can be observed in the estimated fluxes. Coinciding with above analysis, for conventional OFC, the correction points of each flux are updated by two times within one cycle. Due to the low updating frequency, large fluctuation appears in the generated $\hat{d}_\beta$, as shown in Figure 8(b). Specially, the time points of correcting waveform fluctuations are the time points of correcting updates. Besides, additional ripples are introduced into estimated rotor fluxes ($\hat{\psi}_{r\alpha}$ and $\hat{\psi}_{r\beta}$). As a result, the estimation error of rotor position by OFC is 0.6 rad. In Figure 9, the ideal orthogonal sinusoidal signals are observed by IOFC, in which the observation error is 0.002 Wb. As marked in Figure 9, by using IOFC, the correction points of each flux are updated by six times within one cycle. The generated correction term is very smooth for compensation. For proposed IOFC, the rotor position error is reduced to 0.06 rad. There-

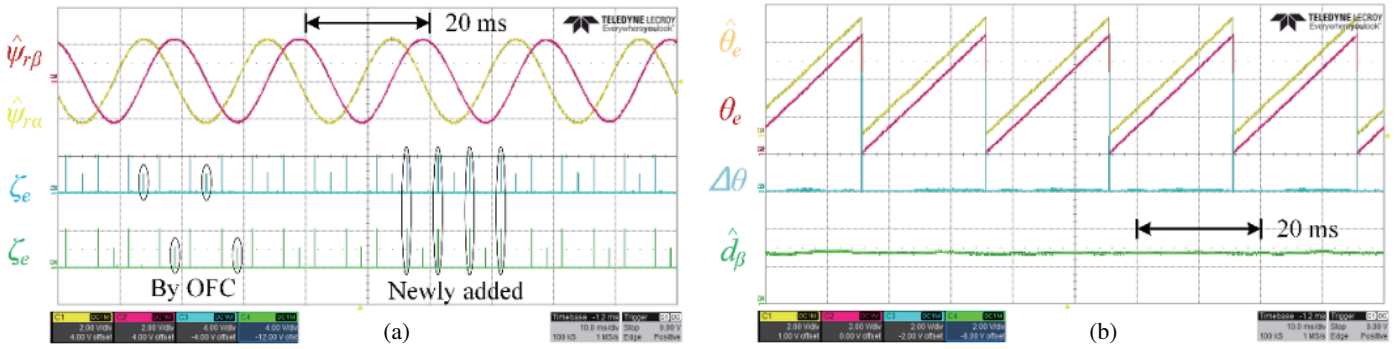

FIGURE 9. Waveforms by IOFC: (a) observed rotor flux and correction points, (b) rotor position and estimated DC component.

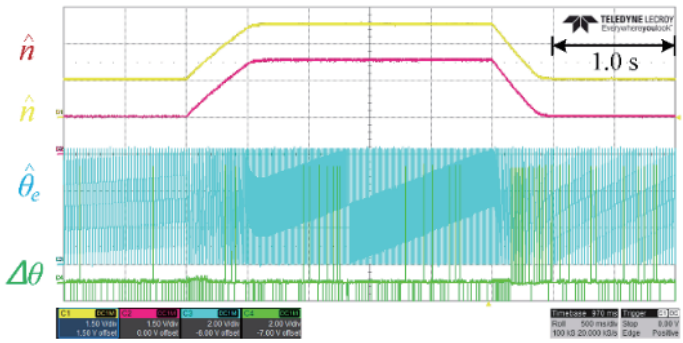

FIGURE 10. Varying speed operation: velocity and rotor position.

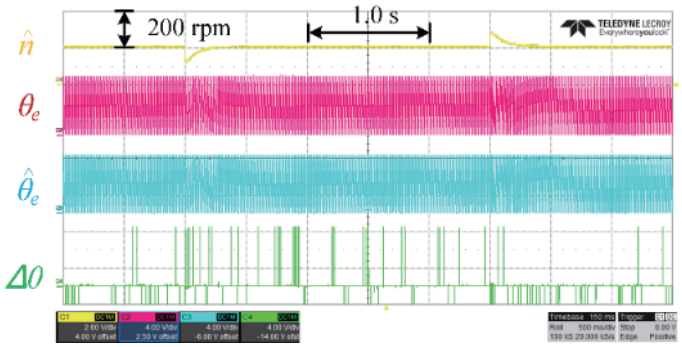

FIGURE 11. Varying load operation: velocity and rotor position.

fore, the smooth correction and fast compensation capabilities of IOFC are verified.

4.2. Performance under Speed & Load Variations

As presented in Figures 10 and 11, the accurate velocity and rotor position can be obtained by IOFC-based method. Here, more experimental waveforms under dynamic varying load and velocity are also provided. In the range of 500 and 1500 rpm, the estimated velocity and rotor position are given in Figure 10. In a long-time scale, the rotor position error is plotted for verification. The rotor position can be acquired with the dynamic estimation error within 0.1 rad. For load-varying condition (12 Nm), the IOFC-based sensorless drive performance is also provided in Figure 11. As the real and estimated rotor positions are presented, the rotor position error is smaller than 0.05 rad.

5. CONCLUSION

By building upon conventional OFC, we establish additional orthogonal signals with double frequency. This facilitates the identification of new conditions that trigger flux correction, consequently increasing the number of rotor flux corrections within one cycle. Moreover, tthis flux observer, characterized by its simple structure, enables compensation of the DC offset in the estimated flux. Leveraging these enhanced flux corrections, we design a PMSM sensorless drive system, which is validated through experimental verifications.

REFERENCES

[1] Liu, X., Y. Pan, Y. Zhu, H. Han, and L. Ji, "Decoupling control of permanent magnet synchronous motor based on parameter identification of fuzzy least square method," *Progress In Electromagnetics Research M*, Vol. 103, 49–60, 2021.

[2] Jiang, Y., W. Xu, C. Mu, J. Zhu, and R. Dian, "An improved third-order generalized integral flux observer for sensorless drive of pmsms," *IEEE Transactions on Industrial Electronics*, Vol. 66, No. 12, 9149–9160, Dec. 2019.

[3] Pan, Y., X. Liu, Y. Zhu, and Z. Li, "A leading angle flux weakening control method for PMSM based on active disturbance rejection control]," *Progress In Electromagnetics Research C*, Vol. 121, 29–38, 2022.

[4] Jiang, Y., W. Xu, C. Mu, and Y. Liu, "Improved deadbeat predictive current control combined sliding mode strategy for PMSM drive system," *IEEE Transactions on Vehicular Technology*, Vol. 67, No. 1, 251–263, Jan. 2018.

[5] Ni, R., D. Xu, F. Blaabjerg, K. Lu, G. Wang, and G. Zhang, "Square-wave voltage injection algorithm for PMSM position sensorless control with high robustness to voltage errors," *IEEE Transactions on Power Electronics*, Vol. 32, No. 7, 5425–5437, Jul. 2017.

[6] Kim, H., J. Son, and J. Lee, "A high-speed sliding-mode observer for the sensorless speed control of a PMSM," *IEEE Transactions on Industrial Electronics*, Vol. 58, No. 9, 4069–4077, Sep. 2011.

[7] Park, Y. and S.-K. Sul, "Sensorless control method for PMSM based on frequency-adaptive disturbance observer," *IEEE Journal of Emerging and Selected Topics in Power Electronics*, Vol. 2, No. 2, 143–151, Jun. 2014.

[8] Dian, R., J. Zhang, and Y. Jiang, "Improved MOGIFO-based flux observation strategy for PMSM sensorless drives," *IEEE Access*,

Vol. 12, 28 475–28 483, Feb. 2024.

[9] Bobtsov, A. A., A. A. Pyrkin, R. Ortega, S. N. Vukosavic, A. M. Stankovic, and E. V. Panteley, "A robust globally convergent position observer for the permanent magnet synchronous motor," *Automatica*, Vol. 61, 47–54, Nov. 2015.

[10] Wu, C., X. Sun, and J. Wang, "A rotor flux observer of permanent magnet synchronous motors with adaptive flux compensation," *IEEE Transactions on Energy Conversion*, Vol. 34, No. 4, 2106–2117, Dec. 2019.

[11] Yu, B., A. Shen, B. Chen, X. Luo, Q. Tang, J. Xu, and M. Zhu, "A compensation strategy of flux linkage observer in SPMSM sensorless drives based on linear extended state observer," *IEEE Transactions on Energy Conversion*, Vol. 37, No. 2, 824–831, Jun. 2022.

[12] Zhao, M., G. Liu, Q. Chen, Z. Liu, X. Zhu, and C. H. T. Lee, "Effective position error compensation in sensorless control based on unified model of SPMSM and IPMSM," *IEEE Transactions on Industrial Informatics*, Vol. 19, No. 5, 6750–6761, May 2023.

[13] Wang, S., D. Ding, G. Zhang, B. Li, Q. Wang, G. Wang, and D. Xu, "Flux observer based on enhanced second-order generalized integrator with limit cycle oscillator for sensorless PMSM drives," *IEEE Transactions on Power Electronics*, Vol. 38, No. 12, 15 982–15 995, Dec. 2023.

[14] Wu, S., C. Hu, Z. Zhao, and Y. Zhu, "High accuracy sensorless control of permanent magnet linear synchronous motors for variable speed trajectories," *IEEE Transactions on Industrial Electronics*, Vol. 71, No. 5, 4396–4406, May 2024.